Miner Deposita (2015) 50:665–674
DOI 10.1007/s00126-014-0562-z

ARTICLE

Quantified, multi-scale X-ray fluorescence element mapping using the Maia detector array: application to mineral deposit studies

Louise A. Fisher · Denis Fougerouse · James S. Cleverley · Christopher G. Ryan · Steven Micklethwaite · Angela Halfpenny · Robert M. Hough · Mary Gee · David Paterson · Daryl L. Howard · Kathryn Spiers

Received: 29 April 2014 / Accepted: 17 October 2014 / Published online: 16 November 2014

Abstract The Maia large solid-angle detector array and imaging system is capable of collecting high-resolution images of up to ~100 M pixels in size with dwell times of less than 0.2 ms per pixel and thus it is possible to document variation in textures associated with trace element chemistry by collecting quantified elemental maps of geological samples on the scale of entire thin sections in a short time frame (6–8 hr). The analysis is nondestructive and allows variation to be recognised on a centimetre scale while also recognising zonations at the micron scale.

Studies of ore systems require microanalysis of samples to collect information on mineral chemistry in order to understand physiochemical conditions during ore genesis and alteration. Such studies contribute to the debate on whether precious metals are remobilised or introduced in multiple hydrothermal events. In this study we demonstrate the microanalytical capabilities of the Maia large solid-angle detector array and imaging system on the X-ray fluorescence microscopy beamline at the Australian Synchrotron to provide data for these studies. We present a series of case studies from orogenic gold deposits that illustrate the power of the Maia detector for constraining chemical zonations in sulphides and associated alteration minerals, which can be used to decipher ore-forming processes associated with gold deposition. A series of large-area (<7 cm^2) elemental maps were collected with 2 to 4 μm pixel size using the Maia detector array. The data was processed using the GeoPIXE™ software package which allows variation in trace, minor and major element chemistry to be visualised in element maps. These maps are used to target further investigation with bulk spectra extracted and fitted for specific mineral grains and transects drawn through regions of interest. Analysis using the Maia detector offers a complementary method to map element distribution in geological samples that is both relatively fast and has a low detection limit for many elements of interest.

Keywords Synchrotron · X-ray fluorescence microscopy · Orogenic gold · Sulphide · Zonation

Editorial handling: R.L. Romer and G. Beaudoin

L. A. Fisher (✉) · J. S. Cleverley · A. Halfpenny · R. M. Hough
CSIRO Mineral Resources Flagship, PO Box 1130, Bentley, WA 6102, Australia
e-mail: louise.fisher@csiro.au

D. Fougerouse · S. Micklethwaite · M. Gee
Centre for Exploration Targeting, The University of Western Australia, Crawley, WA, Australia

C. G. Ryan
CSIRO Mineral Resources Flagship, Gate 5, Normanby Road, Clayton, VIC, Australia

D. Paterson · D. L. Howard · K. Spiers
XFM Beamline, Australian Synchrotron, 800 Blackburn Road, Clayton, VIC, Australia

Present Address:
A. Halfpenny
Electron Microscopy Facility, Department of Imaging and Applied Physics, Curtin University, GPO Box U1987, Perth, WA 6845, Australia

Present Address:
J. S. Cleverley
Reflex, 216 Balcatta Road, Balcatta, WA 6021, Australia

Introduction

Studies of hydrothermal ore systems have traditionally included microanalysis of samples to collect information on mineral chemistry, mineralogy and texture (Cline 2001; Cook et al. 2009, 2011; Large et al. 2009, 2013; Reich et al. 2013; Sung et al. 2009). Information from in situ microcharacterisation studies can be used to recognise both mineral zonations and chemical relationships among mineral phases that provide a

record of hydrothermal activity, fluid chemistry and fluid-rock reactions. Such information is vital in constraining models of ore genesis. Microchemical data also informs metallurgical understanding and subsequent processing of characterised materials (Gregory et al. 2013).

Element mapping of geological materials utilises a range of techniques, with electron probe microanalysis (EPMA), scanning ion imaging using secondary ion mass spectrometry (SIMS) and laser ablation inductively coupled plasma mass spectrometry (LA-ICP-MS) being most common. For all these techniques, there is a trade-off between spot size, or image resolution, the mappable area and the limits of detection for elements measured. LA-ICP-MS provides quantification for a wide range of trace elements with sub-ppm detection levels and can analyse relatively large areas; however, spot sizes are typically between 15 and 50 μm (Morey et al. 2008; Large et al. 2009, 2013; Dare et al. 2014; Vukmanovic et al. 2014), and the technique is destructive to the sample surface. Conversely, while EPMA is capable of a beam spot size of <1 μm, achieving low limits of detection requires high count times, limiting the area that can be mapped over a realistic time frame (Diehl et al. 2012; Reich et al. 2013). The scanning ion imaging method using SIMS has detection limits of 100–300 ppm for most elements, comparable to EPMA, and beam sizes of 2–15 μm are typical (Reich et al. 2013; Kusiak et al. 2013). Maps produced by scanning ion imaging typically have areas smaller than 1000 μm^2. Typically, individual mineral grains or small clusters of grains are analysed in studies of chemical zonations using these techniques. The technique is destructive to the sample surface.

The development of the Maia large solid-angle detector array and integrated real-time processor on the X-ray fluorescence microscopy (XFM) beamline at the Australian Synchrotron allows imaging of complex natural samples at high resolution (2-4 μm pixels) with images beyond 100 M pixels (Paterson et al. 2011; Ryan et al. 2010a, b). Detection limits of 10–100s of ppm are achievable at dwell times of <1 ms. Consequently, it is possible to document variation in textures associated with trace element chemistry by collecting whole thin section elemental maps in a short time frame (6–8 hr). The use of the Maia detector allows all phases in a thin section to be mapped at 2–4 μm resolution with detection limits comparable to, or exceeding, those achieved by EPMA for most elements. The experimental conditions used provide quantified maps for elements with K-emissions (Ca to Zr) and L-emissions (Au, Pb, Hg, W, Bi, U) between 2.0 and 17.5 keV (Ryan et al. 2014). Maia uses full spectral data collection. Elements do not have to be selected prior to measurement because they are identified during peak fitting of the spectra during processing; this is an important distinction from other characterisation techniques such as EPMA and SIMS scanning ion imaging. Most importantly, XFM Maia analysis is nondestructive to the surface of the sample, allowing for follow-up analyses by other techniques such as electron backscatter diffraction (EBSD) or validation of key results against complimentary quantitative element mapping techniques, such as SIMS scanning ion imaging or LA-ICP-MS. Combining these techniques allows the study of high-grade gold deposition in relation to subtle proxies of the previous chemical and microstructural history of the host rocks.

One particular issue hotly debated within economic geology is the source of and deposition mechanisms for high-grade gold in orogenic gold systems (Groves 1993; Large et al. 2009; Phillips and Powell 2010; Tomkins 2013). Analysis of pyrite and other sulphides has underpinned much of this debate. Understanding the distribution of Au and other elements within sulphides can help address many of the questions around ore formation and provide evidence for the timing of Au emplacement. We present three case studies from two orogenic gold deposits. Samples in two of the case studies are taken from the Sunrise Dam Gold Mine (SDGM). Gold at SDGM is contained within quartz-rich veins with little gold observed in the wall rock. Pyrite is the most common sulphide at the deposit and is present in variable amounts in ore zones and within alteration haloes in the country rocks (Yardley and Cleverley 2013). The third case study sample is taken from the Obuasi gold mine. Gold mineralization at Obuasi is contained both in sulphides (mostly arsenopyrite disseminated in the metasedimentary host rock) and as visible gold in quartz veins (Oberthür et al. 1997; Yao and Robb 2000).

These case studies illustrate the potential for Maia element mapping to address questions around Au emplacement and ore formation with data collected over a range of scales (μm to cm). The first and second examples examine the variation in sulphide phases around high-grade gold veins while the third considers the fine-scale alteration of sulphides. These case studies demonstrate the application of the Maia element mapping technique to solve problems relevant to economic geology.

X-ray fluorescence microscopy (XFM) mapping methods

X-ray fluorescence (XRF) microscopy was performed on the XFM beamline at the Australian Synchrotron (Paterson et al. 2011) using the Kirkpatrick-Baez mirror microprobe end-station. This provides a monochromatic 2 μm beam spot size for energies in the range 4–20 keV. Equipped with a Maia 384 detector array, the XFM beamline can acquire full spectral X-ray data for each detector at step sizes down to 2 μm over areas of several square centimetres (Kirkham et al. 2010; Ryan et al. 2010a) with count rates of ~4–10 M/s and energy resolution of 300–400 eV (recent upgrades to Maia 384C provide 240 eV resolution (Ryan et al. 2014)). Analysis of this spectral data, in real-time or in off-line processing, yields quantitative multi-element images with up to 100 M pixels. In

case studies A and B, large-area (4–7 cm^2) element maps were collected on each sample, with an incident beam energy of 18.5 keV, a pixel size of 4 μm and dwell times per pixel of 0.97 ms. The sample in case study C was mapped with a pixel size of 2 μm, dwell time of 7.8125 ms over an area of ~2 mm^2 to permit measurement of trace element concentrations with good counting statistics. Samples were prepared as polished petrographic thin sections of 30 μm thickness mounted on 1 mm-thick glass slides (case studies B and C) or as a 1 mm thick polished rock slab (case study A). The sample in case study C was mounted on a quartz glass slide to avoid the potential impact on As analysis from As present in some normal glass slides. Standard foils (Mn, Fe, Pt and YF_3) were analysed daily to allow calculation of the X-ray flux and monitor drift. X-ray penetration is not limited to a few microns, due to the high energy of the incident beam, so for each pixel, the concentration is an average of the whole volume sampled (Ryan et al. 2014; Dyl et al. 2014).

Maia uses full spectral data collection. Elements do not have to be selected prior to measurement because they are identified during peak fitting of the spectra during processing. The Maia XFM full spectral data were analysed using the GeoPIXE software suite which uses a fundamental parameters approach, with spectral deconvolution and imaging using the dynamic analysis method (Ryan 2000; Ryan et al. 2010b), based on fitting a representative total spectrum and a detailed model of Maia detector array efficiency (Ryan et al. 2010a). Spectra are fitted using X-ray line relative intensities that reflect integration of yields and X-ray self-absorption effects for the given matrix or mineral phase and the contrasting efficiency characteristics across the detector array (Ryan et al. 2010a, b). The result is a matrix transformation that can be used in real-time or off-line projection of full spectral data into element maps. For the samples in this study, whole thin section maps were initially produced by fitting the bulk spectra for the sample. Quantification of trace element concentrations within specific mineral phases was subsequently refined by extraction and refitting of spectra from the mineral phase of interest, with yields calculated using a specific matrix for that mineral.

Results

Case study A

The Maia element maps show multiple sulphide assemblages that are observed in the sample from Sunrise Dam, which represents the contact zone between potassic and sulphide-altered wall rock and a gold-bearing quartz-carbonate vein. Sr, Ca, Fe and Mn maps show thin carbonate veins also cross-cut the wall rock, parallel or sub-parallel to the main vein contact, and these host coarse (1–2 mm) pyrite but contain no measurable gold.

The large-area maps (71×7 mm) of the sample show considerable variation in mineral chemistry moving into the gold-bearing vein (Fig. 1). A population of fine-grained (<200 μm) arsenian pyrite occurs within altered wall rock (Figs. 1 and 2). The coarser pyrite grains that sit within the thin carbonate veins have lower As content (As <0.1 % in bulk pyrite grain analyses) than the wall rock population (0.1–0.25 % As in bulk pyrite grain analyses). The As content in the vein-hosted pyrite is more variable than that in the wall rock pyrite, with As-rich zones mainly formed around cracks in the pyrite grains (Figs. 1 and 2). The wall rock around the thin carbonate-bearing veinlets is bleached, devoid of the fine-grained sulphides within 2–3 mm of the veinlet. Pyrite grains in the gold-bearing quartz vein are coarse and show overgrowing As-enrichment zones, similar to those observed in the thin carbonate veins. Arsenic enrichment around fractures in the coarse pyrite is also observed. The abundance of Cu also varies across the sample. In the wall rock sulphides Cu concentration is low, while in the quartz-rich zones Cu is abundant and mainly associated with As, indicating the presence of tennantite. Tennantite occurs both as free grains within the quartz vein and as inclusions within pyrite grains. Coarse gold grains are hosted by quartz within the vein, and finer-grained gold is present as inclusions within pyrite in the quartz vein and the pyrite veinlets (Fig. 2). Trace element variations are also observed in the non-sulphide rock matrix. Figure 2d shows variation in Sr, Rb and Zr across the wall rock-vein contact. Over a 19.9 mm transect (x-x′) across the contact, the strontium content varies from below detection limit (<10 ppm) to almost 1000 ppm (Fig. 2e). Detection limits depend on counting statistics and, for XFM imaging, scale generally with the inverse square root of the dwell time per point. In the case of this transect, each data point corresponds to a total dwell time of 32 ms over an area of 8×64 $μm^2$.

Case study B

Elemental maps processed from the bulk spectral data from the sample from Sunrise Dam show sulphide bands in a foliated wall rock truncated by a carbonate vein (Fig. 3a). The full section maps of Fe, As and Ca distribution indicate variation in the distribution of As within these sulphide bands across the length scale of the section. On the left side of the carbonate vein, the bands contain extensive, fine-grained (5–150 μm) As-dominant minerals as well as showing As zonation and inclusions within coarser (50–350 μm) pyrite grains (Fig. 3b). On the right side of the vein, the As minerals are much less abundant (Fig. 3c). Arsenic zonation within pyrites appears similar to that within the coarser pyrite on the left side of the vein. Some pyrite grains on the right side of the vein show atoll structures with As-rich cores (Fig. 3c). Fine-grained Au (<5–12 μm) forms inclusions within the pyrite grains on both sides of the vein. When bulk chemical

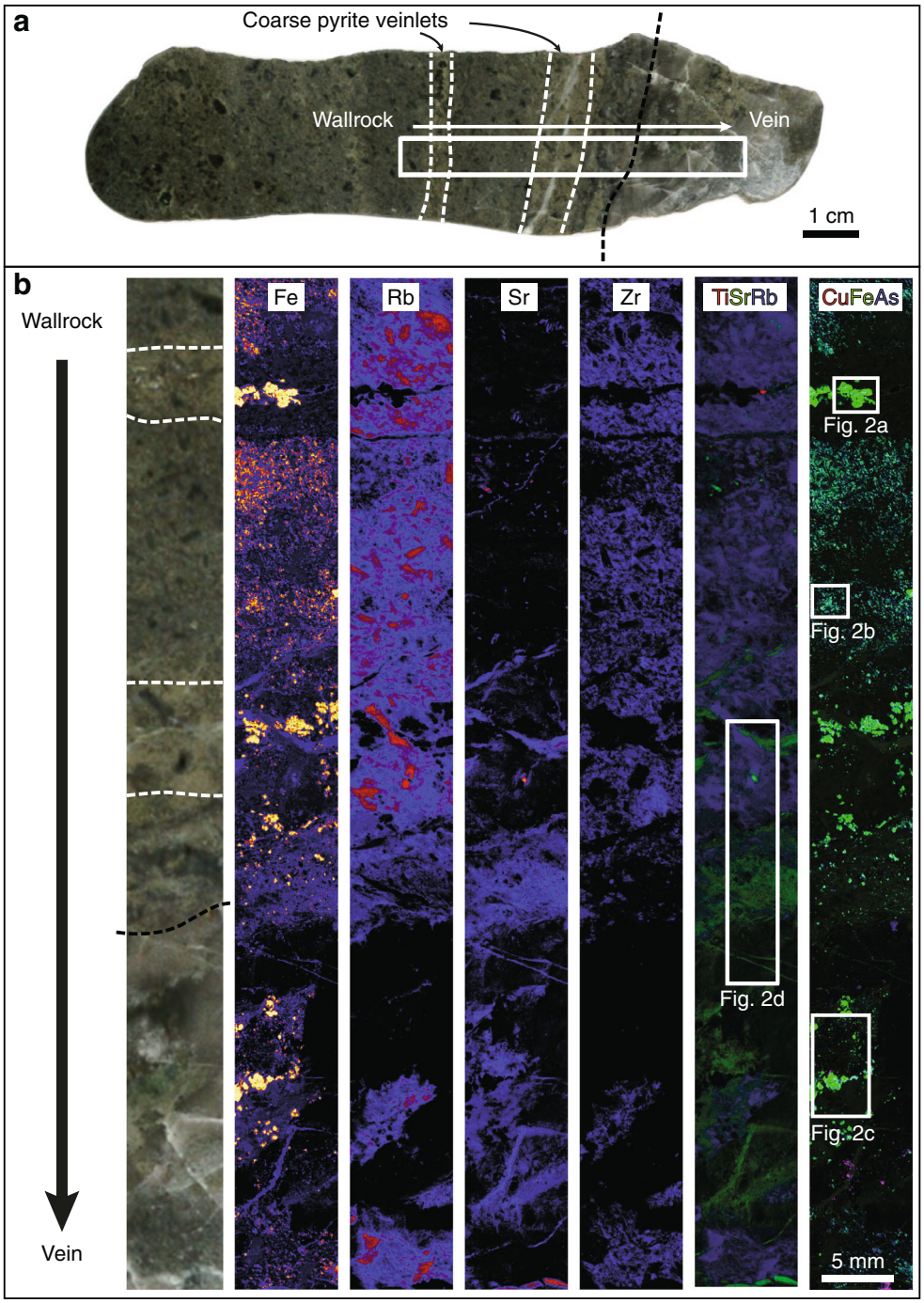

Fig. 1 **a** A slab from Sunrise Dam (case study A—sample GQ1943_3) with the *white box* indicating the area mapped by Maia detector. The *dashed white lines* indicate veinlet margins and the dashed black line indicates the main wallrock-vein contact. **b** Large-area element maps of the sample show heterogeneity in the distribution of elements from wall rock into veins. Individual element maps are presented for Fe, Rb, Sr and Zr. *Black zones* indicate that element was not detected; *blue*, low concentrations; *yellow*, high concentrations. Two RGB composite maps are presented. The subareas shown in Fig. 2 are indicated by *white boxes*. Full-resolution versions of the maps presented in this figure are available through the CSIRO online data repository (Fisher and Ryan 2014)

compositions are extracted for 20 pyrite grains on each side of the carbonate vein, a comparison of As and Cu concentrations in each population shows that Cu concentrations in the pyrite grains on each side of the vein are comparable, between 2000 to 4000 ppm in all grains analysed. Conversely, the As concentrations in pyrite grains on the left reach a maximum of 8.9 wt%, more than double the maximum in pyrite grains on the right side of the vein (Fig. 3d).

Spectra for an arsenian, Au-bearing pyrite (Fig. 4) were extracted and refitted to optimise the quantification (Fig. 4c). Chemical data along a transect (y-y′) through a selected pyrite grain show the variation in As, Cu and Au at 4-μm spacing (Fig. 4). The concentration of arsenic within grain A (Fig. 4) ranges from 0.1 to 6 wt%. Variations in Cu and Zn concentrations in the analysed pyrite grains ranged from <0.1 to 2.5 wt% and <0.04 to 0.75 wt%, respectively. For most features within a 30 μm-thick thin section, it is appropriate to assume a constant composition for the entire thickness of the section. However, for discrete phases with diameters less than the thickness of the section, this does not apply, such as

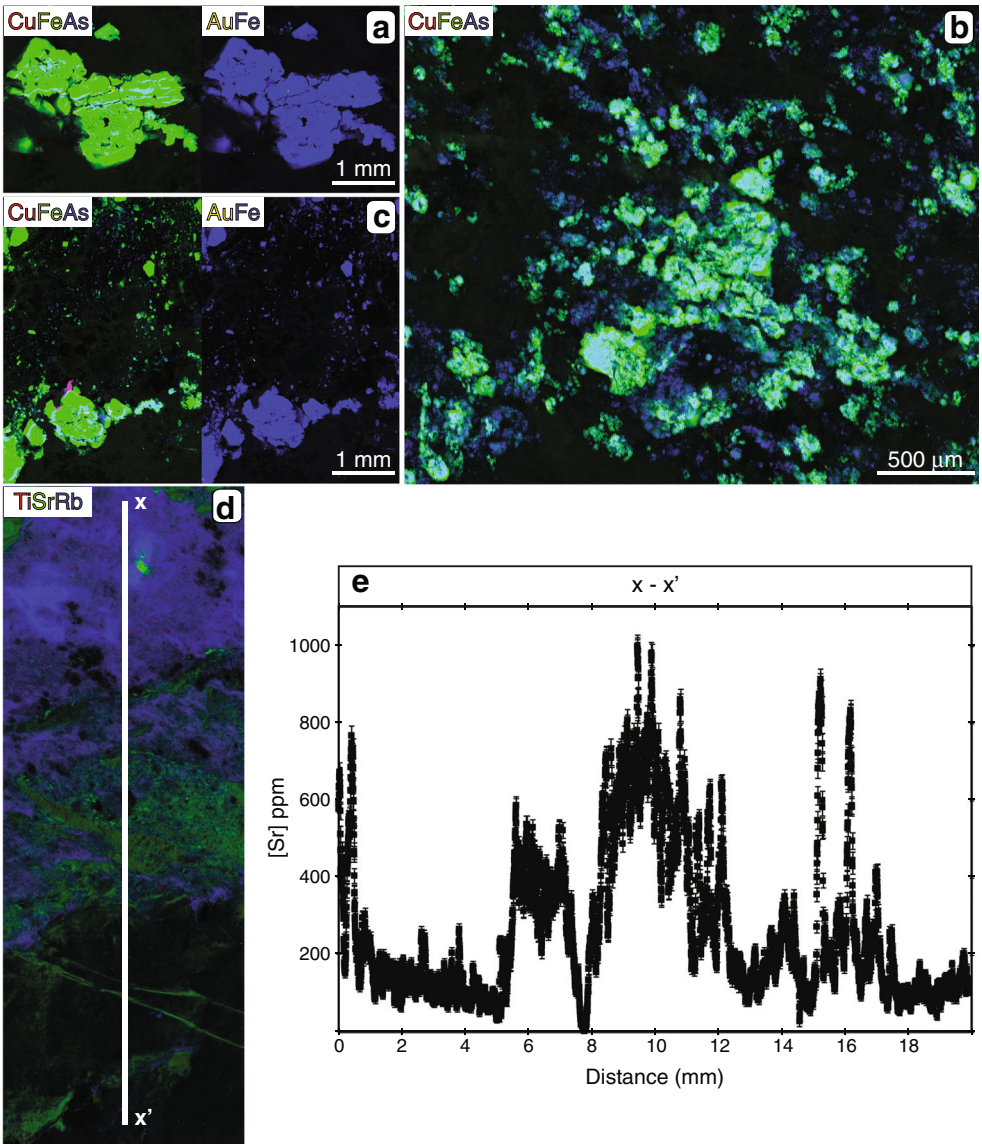

Fig. 2 Selected subareas highlight variation in mineral chemistry and zonation patterns in sulphides across the Sunrise Dam sample in case study A. **a**, **b** and **c** Three different sulphide populations are shown in RGB maps. **d** Trace element variations across the wall rock-vein contact are shown in an RGB map of Rb, Sr and Zr. **e** A transect (x-x^{1}) shows the quantified variation in Sr across the contact and parallel carbonate veinlets. The detection limit for Sr is 10 ppm for a total dwell time of 32 ms per transect point

for small gold grains within sulphides. When a subregion containing Au (largest yellow grain—Fig. 4b) is analysed, initially assuming uniform concentration with depth, a concentration of ~22 wt% Au is measured. This indicates that the full thickness of the thin-section in that pixel is not composed entirely of Au; this therefore indicates either a thin grain of Au at the surface or that Au is present as a discrete, buried phase within the thin section. Petrographic analysis confirms Au is not at the surface of the section, and consequently, the Maia mapping has located a buried phase.

Case study C

Example C is taken from the Obuasi gold mine, and the element map represents an aggregate of euhedral to partially-fragmented arsenopyrite crystals within a mica schist (Fig. 5). Gold mineralization at Obuasi is contained both in sulphides (mostly arsenopyrite disseminated in the metasedimentary host rock) and as visible gold in quartz veins (Allibone et al. 2002). In example C, the distribution of major elements Ca, Fe and As (Fig. 5a) reveals a matrix composed of ankerite, muscovite, chlorite and quartz, whereas the sulphide mineralogy is arsenopyrite with minor pyrite. Figure 5b displays selected trace elements (Au and Ni) concentrated in the sulphides. On the spectra (Fig. 5c), the gold peaks are distinguished in the signal from the arsenopyrite despite the peak overlap and high concentration of arsenic in the sample.

The gold concentration in arsenopyrite ranges from <1000 up to 4000 ppm, contained within multiple, narrow bands that appear to be crystallographically controlled around consistently gold-poor cores (Fig. 5b, d). The arsenopyrite cores are also slightly enriched in Ni. The gold zonation associated with epitaxial overgrowth was previously described using SIMS

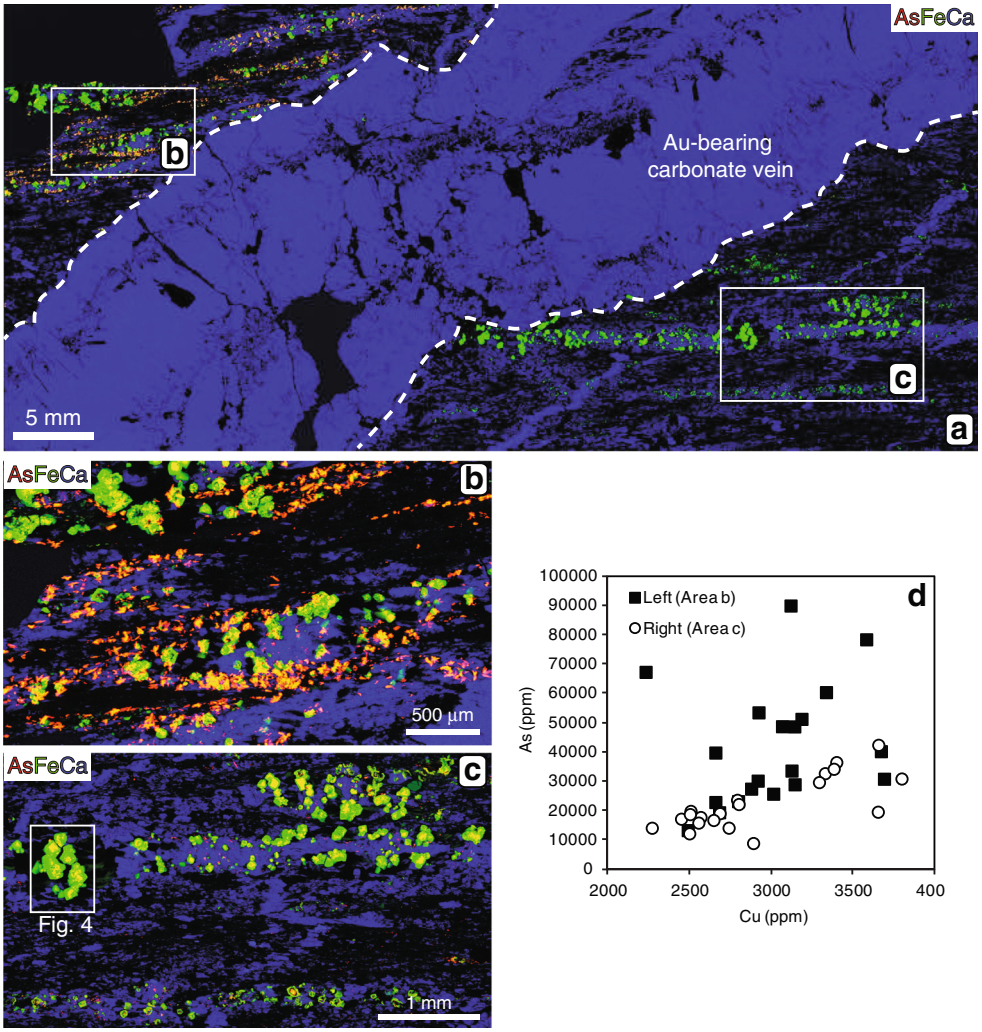

Fig. 3 Maps of the Sunrise Dam sample (WSZ-A) in case study B. **a** Whole thin section element maps of As, Fe and Ca are combined to produce an RGB image (As, *red*; Fe, *green*; Ca, *blue*) of a carbonate vein cross-cutting a foliated wall rock with sulphide banding. Examination of elemental distribution indicates **b** higher As content in the sulphide band in the wall rock on the left of the carbonate vein and **c** lower As content in the sulphide band in the wall rock on the right of the carbonate vein. The *white box* indicates the area shown in Fig. 4. **d** Cu vs. As plot for pyrite from the left (*black square*) and right (*open circle*) sides of the carbonate vein in case study B. Pyrite on the right side shows a relatively constant Cu to As ratio whereas pyrite on left side is relatively enriched in As

scanning ion imaging (Oberthür et al. 1997). In addition to the crystallographically controlled gold, gold grains are found in healed microfractures in the arsenopyrite and pyrite and rarely as inclusions in the arsenopyrite. Nickel concentrations vary in pyrite, defining nickel-rich cores and nickel-poor rims. Nickel also substitutes into narrow rims on limited sections of some arsenopyrite (Fig. 5b).

Along healed microfractures and grain boundaries (Fig. 5), the major and trace element concentrations vary from the bulk mineralogy. Transect z-z′ (Fig. 5d) follows the same primary overgrowth rim (Fig. 5b), demonstrating that arsenic, iron, nickel and gold concentrations vary close to a microfracture at ‘z’, which has been infilled with secondary arsenopyrite. Arsenic and nickel concentrations are higher close to the microfracture (z) whereas the iron and gold concentrations are lower in the same zone. Gold concentrations decrease by approximately 30 %, whereas nickel concentrations change from below the detection limit (75 ppm per transect point) in the rim to up to 4000 ppm close to the fracture.

Discussion

Analysis of samples using the Maia detector and synchrotron radiation is a technique for mapping the distribution of elements of interest in geological samples. It is an effective method for determining the concentrations and distribution of several elements that occur at low-level concentrations. The technique has a broad application in the study of geological materials, both for large-area mapping (e.g. Dyl et al. 2014 mapping of meteorite samples) and locating and mapping the distribution of rare phases such as Au or PGEs (Lintern et al. 2013; Ryan et al. 2013) in geological and biological matrices. Other potential applications include imaging subtle trace element zonations in silicate and carbonate minerals and examination of trace element mobility associated with grain boundaries and microstructures.

Arsenic and antimony are common contaminants in gold and copper processing streams. Similarly, much of the refractory gold in mineral deposits is thought to be ‘invisible’ gold, either nanoparticulate gold or in gold in solid solution within

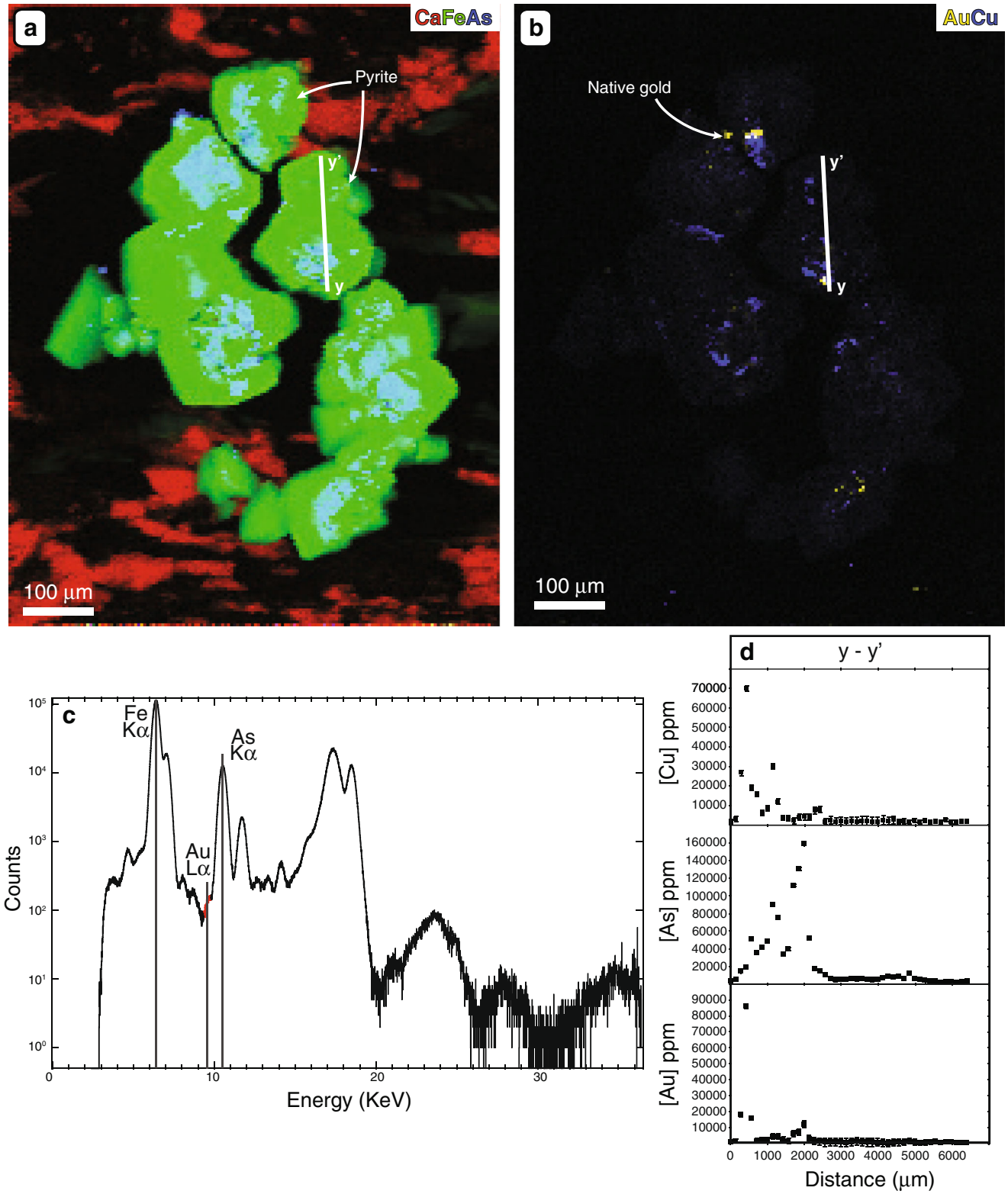

Fig. 4 **a** An RGB image (Ca, *red*; Fe, *green*; As, *blue*) of a subregion containing pyrite grains with As zonation and Au inclusions. **b** Au (*yellow*) and Cu (*blue*) distribution in the same region shown in **a. c** Spectra extracted for a pyrite grain show the presence of the Au (Lα) peak on the shoulder of the As (Kα) peak. **d** Transect y-y[1] through the pyrite grain shows variation in As, Cu and Au concentrations. Detection limits for the elements shown are 278 ppm for Fe, 214 ppm for As and 279 ppm for Au with a total dwell time of 44 ms per transect point

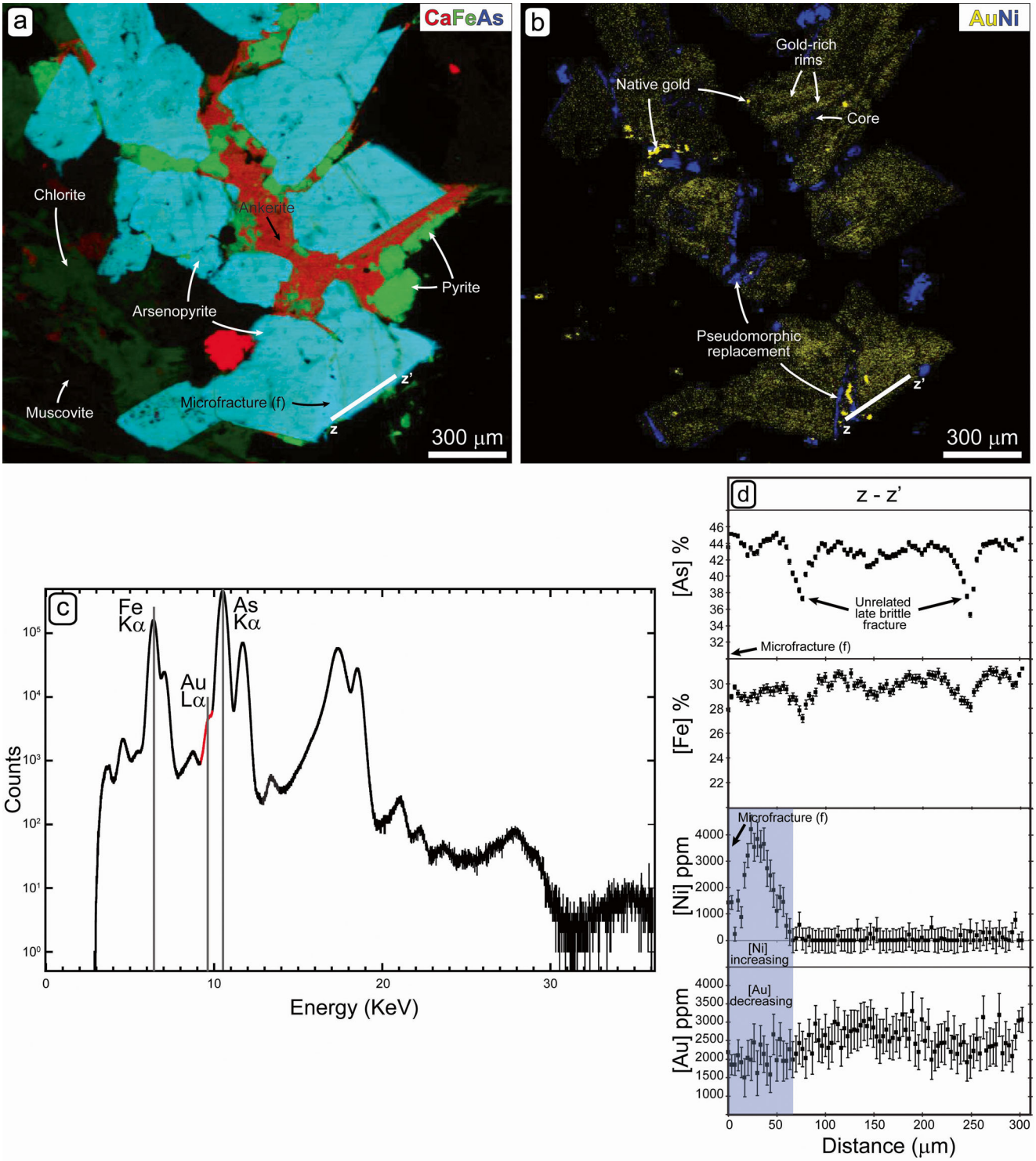

Fig. 5 XFM elemental maps of Obuasi sample 215-7b. **a** An RGB image (*Red*, calcium; *green*, iron; *blue*, arsenic) of a sulphide aggregate. **b** *Yellow*, gold; *blue*, nickel distribution in the same region shown in **a**. The sulphides are pyrites and gold-bearing arsenopyrites. The gold concentration is zoned with higher concentration in epitaxial overgrowth whereas the cores are gold-poor. Nickel is enriched in pyrite cores and along microfractures and grain boundaries in arsenopyrites. The positions of transect z-z^{I} are indicated. **c** XFM spectrum for arsenopyrite grain. Spectra peaks are dominated by iron (Kα) and arsenic (Kα); nevertheless, the resolution available from XFM Maia analysis allows minor peaks and shoulders within the spectra to be positively related to the presence of gold (Lα). **d** As, Fe, Ni and Au concentrations along transect z-z′, the decreases in As and Fe at 70 and 250 mm are due to late brittle fractures. Gold concentration decreases by 30 % adjacent to a microfracture cemented with a secondary arsenopyrite, whereas the nickel concentration is high in the same zone due to pseudomorphic replacement of the primary arsenopyrite

sulphides (Sung et al. 2009; Large et al. 2009; Mackenzie et al. 2014). The knowledge of the distribution of both the value and deleterious elements in ore material is extremely important for evaluating the value of ore and assessing whether these elements also can be extracted or concentrated during mineral processing, feeding into mine and mill planning.

Recognition of trace element variation is also critical for understanding processes of ore formation and hydrothermal alteration. Variations in trace element chemistry and zonation in minerals can record changes in physicochemical conditions during mineral growth. These variations can be fully recognised through high-resolution, whole-section mapping using XFM and the Maia detector. The case studies presented in this contribution demonstrate the application of this method to sulphide chemistry; this technique is, however, applicable to many mineral phases. In case studies A and B, variations in As and Cu content coupled with textural and grain size observations allow multiple populations of pyrite to be discriminated, which can be used to interpret the fluid-rock reaction history with implications for genetic models. Initial wall rock alteration in the sample in case study A is characterised by a potassic overprint with extensive As-rich fine-grained pyrite. Cross-cutting veins are associated with the dissolution of pyrite, with fine-grained pyrite absent around veinlets and precipitation of coarse-grained pyrite with lower bulk As content within the veinlets. The pyrite is subsequently overgrown and overprinted with further enrichment of As in overgrowth zones and along fractures in the coarse-grained pyrite. The veining event associated with coarse gold emplacement seen in case study A is also associated with Cu, forming sulphosalts. Inclusions of Au and sulphosalts within the later, coarse pyrites indicate that this population of pyrite formed contemporaneously with Au emplacement.

Arsenic is an effective pathfinder for Au in many orogenic gold systems. However, the textural observations of As, Cu and Au distribution in pyrite in this study indicate that there were multiple fluid events that mobilised these elements to different degrees. The variation in As in the pyrite grains on either side of the carbonate vein in case study B indicates that As-rich fluids flowed along permeable horizons within the foliated wall rock. Whereas coarse gold is mainly localised within veins, the presence of fine-grained Au inclusions in As-rich pyrite in the wall rock indicates that the As-rich fluids may also have been Au bearing.

The variation in major and trace elements associated with microfracture and grain boundaries in case study C is interpreted as indicating that gold concentration has been modified from the primary zoning of the grains by pseudomorphic replacement (Harlov et al. 2005; Putnis 2009). Oberthür et al. (1997) previously described gold distribution in arsenopyrite at Obuasi using SIMS scanning ion imaging, attributing the highest concentrations of gold to the epitaxial overgrowth of the arsenopyrite grains. However, the studies were restricted by the limitations of the scanning ion imaging technique at that time to a 30 μm spot size and a map area of 120 μm in diameter. In contrast, individual arsenopyrite grains at Obuasi are often up to 1 mm across, and full characterisation of the gold textures in the grains requires resolution at the micrometre scale. The high spatial resolution (2 μm spot size) and multi-element analytical capability that XFM Maia analysis provides are tools to understand complex mineral and alteration relationships over large sample areas of several square centimetres. Data collected can be binned over a range of length scales allowing for chemical quantification of both micro- and macro-features. An advantage of Maia XFM analysis is the ability to detect micrometre-scale grains at any depth within sections of 10s of microns in thickness with an image with spatial resolution determined by the beam spot size (Ryan et al. 2013). This permits distinction between Au inclusions within pyrite and dispersed Au in the matrix of the sulphide and even the determination of particle depth.

Summary and conclusions

The Maia detector on the XFM beamline at the Australian Synchrotron allows collection of high-resolution elemental maps over whole thin sections with detection limits for many trace elements that are comparable with, or better than, EPMA. The step change in mappable area and resolution of this method, compared with EPMA, LA-ICP-MS or SIMS scanning ion imaging analysis, offers the opportunity to fully recognise and quantify variation in mineral chemistry in a sample from whole section length scales to micron scales and to not miss rare precious metal phases located at depth within a sample section.

Maia uses full spectral data collection. Elements do not have to be selected prior to measurement because they are identified during peak fitting of the spectra during processing; this is an important distinction from other characterisation techniques such as EPMA and SIMS scanning ion imaging. Most importantly, Maia XFM analysis is nondestructive allowing for follow-up analyses using other techniques such as electron backscatter diffraction (EBSD) or validation of key results against other quantitative element mapping techniques such as SIMS or LA-ICP-MS.

Acknowledgments This research was undertaken on the X-ray fluorescence microscopy beamline at the Australian Synchrotron, Victoria, Australia. The data presented in this paper were collected as part of run 6666 (Obuasi), 6189 and 4898 (Sunrise Dam) at XFM. Martin de Jonge (XFM beamline scientist) developed scan software and scripts that supported data collection. Micklethwaite and Fougerouse wish to gratefully acknowledge the support of the WAXI stage-2 AMIRA project (P934A) and an ARC linkage grant LP110100667. The Obuasi data forms part of Fougerouse's PhD work which is supported by AngloGold Ashanti. The authors thank Steve Barnes and Belinda Godel for their constructive comments on a draft of this manuscript. We thank Rolf Romer and an anonymous reviewer for their constructive reviews of this manuscript. This research is supported by the Science and Industry Endowment Fund.

References

Allibone AH, McCuaig TC, Harris D, Etheridge M, Munroe S, Byrne D, Amanor J, Gyapong W (2002) Structural controls on gold mineralisation at the Ashanti Gold Deposit, Obuasi, Ghana. SEG Spec Publ 9:29

Cline JS (2001) Timing of gold and arsenic sulfide mineral deposition at the Getchell carlin-type gold deposit, north-central Nevada. Econ Geol 96:75–89

Cook NJ, Ciobanu CL, Danyushevsky LV, Gilbert S (2011) Minor and trace elements in bornite and associated Cu-(Fe)-sulfides: a LA-ICP-MS study. Geochim Cosmochim Ac 75:6473–6496

Cook NJ, Ciobanu CL, Pring A, Skinner W, Shimizu M, Danyushevsky L, Saini-Eidukat B, Melcher F (2009) Trace and minor elements in sphalerite: a LA-ICPMS study. Geochim Cosmochim Ac 73:4761–4791

Dare SAS, Barnes S-J, Pritchard HM, Fisher PC (2014) Mineralogy and geochemistry of Cu-rich ores from the McCreedy East Ni-Cu-PGE Deposit (Sudbury, Canada): implications for the behavior of platinum group and chalcophile elements at the end of crystallisation of a sulfide liquid. Econ Geol 109:343–366

Diehl SF, Goldhaber MB, Koenig AE, Lowers HA, Ruppert LF (2012) Distribution of arsenic, selenium, and other trace elements in high pyrite Appalachian coals: evidence for multiple episodes of pyrite formation. Int J Coal Geol 94:238–249

Dyl KA, Cleverley JS, Bland PA, Ryan CG, Fisher LA, Hough RM (2014) Quantified, whole section trace element mapping of carbonaceous chondrites by Synchrotron X-ray fluorescence microscopy: 1. Oxidised and reduced CV meteorites. Geochim Cosmochim Ac 134:100–119

Fisher LA, Ryan CG (2014) GeoPIXE element maps of sample GQ1943_3. CSIRO. Data Collect. doi:10.4225/08/543DFA47E9878

Gregory MJ, Lang JR, Gilbert S, Olson Hoal K (2013) Geometallurgy of the pebble porphyry copper-gold-molybdenum deposit, Alaska: implications for gold distribution and paragenesis. Econ Geol 108:463–482

Groves DI (1993) The crustal continuum model for late-Archaean lode-gold deposits of the Yilgarn Block, Western Australia. Miner Deposita 28:366–374

Harlov DE, Wirth R, Förster H-J (2005) An experimental study of dissolution–reprecipitation in fluorapatite: fluid infiltration and the formation of monazite. Contrib Mineral Petr 150:268–286

Kirkham R, Dunn PA, Kucziewski A, Siddons DP, Dodanwela R, Moorhead G, Ryan CG, De Geronimo G, Beuttenmuller R, Pinelli D, Pfeffer M, Davey P, Jensen M, Paterson D, de Jonge MD, Kusel M, McKinlay J (2010) The Maia spectroscopy detector system: engineering for integrated pulse capture, low-latency scanning and real-time processing. AIP Conf Proc 1234:240–243

Kusiak M, Whitehouse MJ, Wilde SA, Nemchin AA, Clark C (2013) Mobilisation of radiogenic Pb in zircon revealed by ion imaging: implications for early Earth geochronology. Geology 41:291–294

Large RR, Danyushevsky L, Hollit C, Maslennikov V, Meffre S, Gilbert S, Bull S, Scott R, Emsbo P, Thomas H, Singh B, Foster J (2009) Gold and trace element zonation in pyrite using a laser imaging technique: implications for the timing of gold in orogenic and carlin-style sediment-hosted deposits. Econ Geol 104:635–668

Large RR, Meffre S, Burnett R, Guy B, Bull S, Gilbert S, Goemann K, Danyushevsky L (2013) Evidence for an intrabasinal source and multiple concentration processes in the formation of the carbon leader reef, Witwatersrand Supergroup, South Africa. Econ Geol 108:1215–1241

Lintern M, Anand A, Ryan C, Paterson D (2013) Natural gold particles in Eucalyptus leaves and their relevance to exploration for buried gold deposits. Nat Commun 4:2614. doi:10.1038/ncomms3614

MacKenzie D, Craw D, Finnigan C (2014) Lithologically controlled invisible gold, Yukon, Canada. Mineral Deposita. doi:10.1007/s00126-014-0532-5

Morey AA, Tomkins AG, Bierlein FP, Weinberg RF, Davidson GJ (2008) Bimodal distribution of gold in pyrite and arsenopyrite: Examples from the Archean Boorara and Bardoc shear systems, Yilgarn Craton, Western Australia. Econ Geol 103:599–614

Oberthür T, Weiser T, Amanor JA, Chryssoulis SL (1997) Mineralogical siting and distribution of gold in quartz veins and sulfide ores of the Ashanti mine and other deposits in the Ashanti belt of Ghana: genetic implications. Mineral Deposita 32:2–15

Paterson D, de Jonge MD, Howard DL, Lewis W, McKinlay J, Starritt A, Kusel M, Ryan CG, Kirkham R, Moorhead G, Siddons DP (2011) The X-ray flurorescence microscopy beamline at the Australian Synchroton. AIP Conf Proc 1365:219–222

Phillips GN, Powell R (2010) Formation of gold deposits: a metamorphic devolatilization model. J Metamorph Geol 28:689–718

Putnis A (2009) Mineral replacement reactions. Rev Mineral Geochem 70:87–124

Reich M, Deditius A, Chryssoulis S, Li J-W, Ma C-Q, Parada MA, Barra F, Mittermayr F (2013) Pyrite as a record of hydrothermal fluid evolution in a porphyry copper system: a SIMS/EMPA trace element study. Geochim Cosmochim Ac 104:42–62

Ryan CG (2000) Quantitative trace element imaging using PIXE and the nuclear microprobe. Int J Imag Syst Tech 11:219–230

Ryan CG, Kirkham R, Hough R, Moorhead G, Siddons D, de Jonge M, Paterson D, De Geronimo G, Howard D, Cleverley J (2010a) Elemental X-ray imaging using the Maia detector array: the benefits and challenges of large solid-angle. Nucl Instrum Method A 619:37–43

Ryan CG, Siddons DP, Kirkham R, Dunn PA, Kuczewski A, Moorhead G, De Geronimo G, Paterson DJ, de Jonge MD, Hough RM, Lintern MJ, Hoard DL, Kappen P, Cleverley J (2010b) The new Maia detector system: methods for high definition trace element imaging of natural material. In: Denecke MA, Walker CT (eds). X-Ray Optics and Microanalysis. AIP Conf Proc 1221:9–17

Ryan CG, Siddons DP, Kirkham R, Li ZY, de Jonge MD, Paterson DJ, Cleverley JS, Kuczewski A, Dunn PA, Jensen M, De Geronimo G, Howard DL, Godel B, Dyl KA, Fisher LA, Hough RH, Barnes SJ, Bland PAM, Moorhead G, James SA, Spiers KM, Falkenberg G, Boesenberg U, Wellenreuther G (2013) The Maia detector array and x-ray fluorescence imaging system: locating rare precious metal phases in complex samples. Proc SPIE 8851:88510Q. doi:10.1117/12.2027195

Ryan CG, Siddons DP, Kirkham R, Li ZY, de Jonge MD, Paterson DJ, Kuczewski A, Howard DL, Dunn PA, Falkenberg G, Boesenberg U, De Geronimo G, Fisher LA, Halfpenny A, Lintern MJ, Lombi E, Dyl KA, Jensen M, Moorhead GF, Cleverley JS, Hough RM, Godel B, Barnes SJ, James SA, Spiers KM, Alfeld M, Wellenreuther G, Vukmanovic Z, Borg S (2014) Maia X-ray fluorescence imaging: capturing detail in complex natural samples. X-Ray Optics and Microanalysis. J Phys Conf Ser 499:012002

Sung YH, Brugger J, Ciobanu CL, Pring A, Skinner W, Nugus M (2009) Invisible gold in arsenian pyrite and arsenopyrite from a multistage Archaean gold deposit: Sunrise Dam, Eastern Goldfields Province, Western Australia. Mineral Deposita 44:765–791

Tomkins AG (2013) On the source of orogenic gold. Geology 41:1255–1256

Vukmanovic Z, Reddy SM, Godel B, Barnes SJ, Fiorentini ML, Barnes SJ, Kilburn MR (2014) Relationship between microstructures and grain-scale trace element distribution in komatiite-hosted magmatic sulfide ores. Lithos 184–187:42–61

Yao Y, Robb LJ (2000) Gold mineralization in Palaeoproterozoic granitoids at Obuasi, Ashanti region, Ghana: ore geology, geochemistry and fluid characteristics. S Afr J Geol 103:255–278

Yardley BWD, Cleverley JS (2013) The role of metamorphic fluids in the formation of ore deposits. In: Jenkin et al. (eds) Ore deposits in an evolving Earth. Geol Soc London Spec Publ 393. doi:10.1144/SP393.5